Pore size dependent connectivity and ionic transport in saturated cementitious materials

Zhang, Yong; Ye, Guang; Yang, Zhengxian

DOI
10.1016/j.conbuildmat.2019.117680

Publication date
2020

Document Version
Accepted author manuscript

Published in
Construction and Building Materials

Pore size dependent connectivity and ionic transport in saturated cementitious materials

Yong Zhang [1,2,3], Guang Ye [3], Zhengxian Yang [1,2,*]

[1] Fujian Provincial University Research Center for Advanced Civil Engineering Materials, Fuzhou University, Fuzhou 350116, China;

[2] College of Civil Engineering, Fuzhou University, Fuzhou 350116, China;

[3] Microlab, Section of Materials and Environment, Department of 3MD, Faculty of Civil Engineering and Geosciences, Delft University of Technology, Stevinweg 1, 2628 CN Delft, The Netherlands; y.zhang-1@tudelft.nl (Yong Zhang), g.ye@tudelft.nl (Guang Ye)

* Correspondence: zxyang@fzu.edu.cn (Zhengxian Yang)

Abstract: Microstructure-property relationship has drawn strong attention in modern material science. The progress achieved in this field relies on a common basis that the material performance originates from the microstructure. This paper brings together new insights and facts from experiments regarding the pore size dependent connectivity and its relation to ionic transport property in saturated cementitious materials. An innovative measurement, i.e. intrusion-extrusion cyclic mercury porosimetry (IEC-MIP), is proposed to distinguish between the small capillary pores that are present within clusters of hydration products and the large capillary pores that are left out of hydration products. The distribution of connectivity as a function of pore size in cementitious materials is analyzed. A novel transport parameter, i.e. connectivity of small capillary pores, is introduced and quantified by IEC-MIP measurements. The ionic transport was measured by means of rapid chloride migration tests. A power relationship is established between connectivity of small capillary pores and chloride migration coefficient for cementitious materials irrespective of the binder type.

Keywords: Pore connectivity; Chloride transport; Mercury porosimetry; Intrusion–extrusion; Cementitious material

1. Introduction

The increasing awareness on sustainability of building infrastructures makes it necessary for researchers and engineers to pay more attention on the durability of concrete structures. A major

durability concern nowadays for marine concrete structures can be ascribed to the chloride-induced reinforcement corrosion, caused by chloride penetration into concrete through the interconnected pore network. An in-depth understanding of the relationship between chloride penetration and microstructure is an essential step toward reliable design of durable marine concrete [1,2].

Hardened cement matrix contains a variety of pore types. Calcium silicate hydrates (C-S-H), which are the main hydration products, contain molecular-scale interlayer pore space and nanometric gel pores (≤ 10 nm) [3]. The micrometric capillary pores (10 nm ~ 10 μm), usually irregular in shape, are formed due to insufficient packing of the hydration products, and represent the originally water filled space [4]. According to different refinement mechanism, two types of capillary pores have been distinguished [4-5]: *small* capillary pores referring to void space present within clusters of hydration products and *large* capillary pores accounting for void space left out of hydration products. With ongoing cement hydration, the hydration products are precipitated in the capillary pores. Each cement grain grows outward until contact with neighboring cement grain, initiating so called contact area [5] as marked in the hydration cell (Fig. 1a). The contact area is enlarged with a higher degree of cement hydration.

The percolation theory, proposed by Bentz [6] who explained mass transport against the connectivity of capillary pores, has been long time applied to study the transport property in porous media. Pore connectivity is a scalar quantity and stands for a relatively accessible variable. In hydrated cementitious systems the capillary pores are distributed with different pore geometry. A typical classification of the pore geometry is schematically illustrated in Fig. 1b [7]: (i) continuous pores, which can make up an interconnected network relating the two opposite surfaces of a specimen; (ii) dead-end (ink-bottle) pores, which are connected with only one surface of a specimen; (iii) isolated pores, which are surrounded by solid phases and have no connection with any surface of a specimen. The isolated pores have no impact on mass transport, they are therefore not of interest in usual pore structure analysis. Both continuous pores and dead-end (ink-bottle) pores contribute to the total open porosity, but the mass transport is predominantly controlled by the continuous pores.

Figure 1. (a) Hydration cell of two cement grains; (b) Pore geometry for (i) continuous pore, (ii) dead-end (ink-bottle) pore and (iii) isolated pore.

A complete description and detailed characterization of the pore connectivity in cementitious materials is a topic of considerable efforts. The ratio of connected porosity over total porosity, termed as *overall connectivity* η_{p} hereafter, was routinely analyzed in most previous reports [7-14]. Conventional relationships, such as Archie's law [15] for resistivity and Darcy's law [16] for permeability, were established based on well-connected pore network. These relationships have been found imperfect [17,18], especially for cementitious materials whose pore network is not well-connected or being in unsaturated state [19]. Navi and Pignat [7] simulated the tricalcium silicate microstructure using an integrated particle kinetics model and examined the pore connectivity in detail. The voxel-based CEMHYD3D model proposed by Bentz [20], referred to by Liu et al. [21], and the vector-based HYMOSTRUC3D model [5,22], referred to by Zhang et al. [23], were implemented to simulate the connectivity of capillary pores, and the pore volume at which depercolation of capillary pores takes place was figured out.

Mercury intrusion porosimetry (MIP) technique is widely used at present, although some assumptions and simplifications are required for interpretation of the pore structure data measured [24]. MIP measures the pore sizes based on the accessible throat (continuous pores) to reach internal ink-bottle pores [25]. This accessibility issue, along with other limitations, has been well documented by Diamond [26]. Nevertheless, MIP tests are appropriate to identify such pore features as accessible porosity (noted as total open porosity occasionally), effective porosity, ink-bottle porosity and threshold pore diameter [19,22,26]. The overall connectivity η_{p} was often estimated as the quotient of the effective porosity over the total open porosity, as described by Garboczi [27]. X-ray computed microtomography (X-CT), together with 3D image analysis, was employed by Zhang et al. [23] and Promentilla et al. [28], among others, to analyze the η_{p} value. Resolution limitation of X-CT, e.g. 0.5 μm, makes it difficult to truthfully capture the connectivity of nano pores in cementitious materials. Transmission X-ray Microscope (TXM) with a resolution as high as 0.03 μm has been reported for determining the η_{p} value [29]. Zhou et al. [30] investigated the η_{p} by means of focused ion beam scanning electron microscopy (FIB-SEM), in combination with the 3D pore structure reconstruction. Nuclear magnetic resonance (NMR) enables to measure the total pore volume including connected pores and disconnected pores (isolated pores) in water-saturated cementitious materials. Gao et al. [31] examined the fraction of the open pore voids (from MIP) over the total pore voids (from NMR) to determine the connectivity value, but that the continuous pores and the ink-bottle pores were not differentiated.

The pores of different size play a different role in mass transport property. To what extent the connectivity and the pore size can be correlated remains an open question, because of the

intricate microstructural characteristics and associated complex pore morphology, and also due to the wide range of pore size distribution covering nearly six orders of magnitude. None of the existing models/equations about pore connectivity can account for the full body of the experimentally obtained transport results reported in literature [1]. The overall connectivity η_{p} is a global parameter that was launched to stand for connectivity of the pores over entire pore size range in a porous medium. A relationship between overall connectivity η_{p} and mass transport property can be judged valid *only* when all pore voids, irrespective of pore size, are entirely and equally important for mass transport. This is, however, not the case for cementitious materials, where the connected pores allowing for mass transport can be divided into one part that dominates the mass transport and another part that plays little role. Pore blocking and cavitation in cementitious materials highly influence the mass transport in view of absorption, desorption and sorption hysteresis [32-34].

Mercury porosimetry has a significant potential for a comprehensive understanding of the pore structure owing to the suitability for a broad pore size identification. With the assumption that dead-end (ink-bottle) pores remain filled with entrapped mercury after completion of the 1st mercury intrusion-extrusion cycle, no remaining mercury is expected when performing the 2nd cycle [35]. In the present work an alternative measurement, namely *intrusion-extrusion cyclic mercury porosimetry* (IEC-MIP), is introduced, with which the continuous pores and the ink-bottle pores can be distinguished and meanwhile a clear picture of the pore connectivity at different scales in cementitious materials is acquired. A range of water-binder-ratio (0.4～0.6) and supplementary cementitious materials, such as fly ash, ground granulated blast furnace slag and limestone powder, were considered for specimen preparation. A novel transport parameter, *connectivity of small capillary pores*, is put forward and quantitatively characterized, whose relevance to the ionic transport property as indicated by rapid chloride migration tests will be demonstrated by the experimental data.

2. Experimental

2.1. Materials and samples

Raw materails under study were ordinary Portland cement CEM I 42.5N (OPC) and supplementary cementitious materials (SCMs) including low-calcium fly ash (FA), limestone powder (LP) and ground granulated blast furnace slag (BFS). Cement paste and mortar samples were prepared. A fixed sand/binder ratio of 3 was used. The mixing process was controlled in accordance with EN 196-1 [36]. The binder mixtures included pure OPC, binary and ternary

cements. Substitutions of the OPC with blends by mass percentage were at dosage levels of 30%, 70% and 5% for FA, BFS and LP, respectively. The water-binder-ratio (w/b) varied from 0.4 to 0.6. Details of the mixture proportions are given in Table 1. The densities of the raw materials were 3.12 g/cm^3 for OPC, 2.26 g/cm^3 for FA, 2.87 g/cm^3 for BFS and 3.08 g/cm^3 for LP.

Table 1. Mix proportions for paste and mortar samples (weight percentage) with ordinary Portland cement (OPC), fly ash (FA), ground granulated blast furnace slag (BFS) and limestone powder (LP).

The paste samples were cured under sealed condition for 28, 105, 182 and 370 days. At each desired age, the paste samples were split into small pieces (around 1 cm^3). Regarding all the methods to dry cement pastes for pore structure analysis, the liquid nitrogen freeze-drying method has the minimum damage. In this respect two very typical studies can be found elsewhere in Refs. [22,37]. In this work, liquid nitrogen was used to stop further hydration of the paste pieces. Then these paste pieces were moved into a freeze-dryer at −24 ˚C and under vacuum at 0.1 Pa. The paste pieces were ready for pore structure measurements after mass loss of water was below 0.01% per day. Cylindrical mortar samples were cast and moist-cured at 20 ± 1 ˚C. The mortar samples were conditioned for rapid chloride migration tests at ages of 28, 105, 182, 370 and 730 days.

2.2. Pore structure characterization by intrusion-extrusion cyclic mercury porosimetry (IEC-MIP)

In standard mercury intrusion porosimetry (MIP) test, mercury is forced to penetrate into the pore system of a specimen by increasing the applied pressure from the minimum to the maximum. Assuming the pores are cylindrical in shape, the correlation between the applied pressure P [MPa] and the pore diameter d [μm] can be described with the Washburn equation [38]:

$$d = (-4\gamma_{\mathrm{Hg}}\cos\theta)/P \quad (1)$$

where γ_{Hg} (0.48 N/m) is the surface tension of the mercury; θ (139°) is the contact angle between mercury and pore wall.

159 It is well known that the standard MIP suffers from the ink-bottle effect, resulting in an
160 overestimation of small capillary pores and an underestimation of large capillary pores [25,26].
161 In this work an alternative measurement procedure, named *intrusion-extrusion cyclic mercury*
162 *porosimetry* (IEC-MIP), is proposed for pore structure characterization. The IEC-MIP enables
163 to deeply understand the ink-bottle effect and distinguish between small capillary pores and large
164 capillary pores. The IEC-MIP measurement was composed of one low-pressure intrusion step
165 (from 0 to P_0 = 0.15 MPa) and twenty high-pressure intrusion steps (stepwise from P_0 = 0.15 to
166 210 MPa). Each high-pressure intrusion step was followed by an extrusion procedure. At each
167 intrusion step, mercury was forced to penetrate the microstructure through the small (throat)
168 pores to reach the internal large (ink-bottle) pores. At the subsequent extrusion step, only
169 mercury in the small (throat) pores was extruded while mercury in the large (ink-bottle) pores
170 was irreversibly entrapped (Fig. 2).
171

172 Figure 2. Mercury intrusion-extrusion hysteresis in a pore system with a throat pore connecting
173 an ink-bottle pore.

174

175 Fig. 3a illustrates the test sequence of the IEC-MIP measurement. At intrusion step i-1, the
176 applied pressure was increased from P_0 to $P_{i\text{-}1}$. The minimum intrusion pore diameter was $d_{i\text{-}1}$
177 and the cumulative intrusion volume was V_{i-1}^{cin}. At extrusion step i-1, the applied pressure was
178 decreased from $P_{i\text{-}1}$ to P_0 and the cumulative ink-bottle volume was V_{i-1}^{cink}. At intrusion step i,
179 the applied pressure was increased from P_0 to P_i, corresponding to intrusion pore diameter d_i and
180 cumulative intrusion volume V_i^{cin}. At extrusion step i, the cumulative ink-bottle volume was
181 V_i^{cink}.

182

183 Figure 3. (a) Test sequence of intrusion-extrusion cyclic mercury porosimetry (IEC-MIP): from
184 step (i-1) to step i, the cumulative intrusion volume increases from V_{i-1}^{cin} to V_i^{cin} and the
185 cumulative ink-bottle volume increases from V_{i-1}^{cink} to V_i^{cink}; (b) Standard mercury intrusion
186 porosimetry (MIP), consisting of an intrusion from the minimum to the maximum pressure and
187 an extrusion from the maximum to the minimum pressure, and the 2nd intrusion.

188

From intrusion step *i*-1 to *i*, mercury fills the throat pores (diameter d_i, volume V_i^{th}) and the neighboring ink-bottle pores (volume V_i^{ink}). Both V_i^{th} and V_i^{ink}, as well as the connectivity η_i, at the specific pore diameter d_i can be expressed with Eqs. (2), (3) and (4), respectively.

$$V_i^{\mathrm{th}} = \left(V_i^{\mathrm{cin}} - V_{i-1}^{\mathrm{cin}}\right) - \left(V_i^{\mathrm{cink}} - V_{i-1}^{\mathrm{cink}}\right) \quad (2)$$

$$V_i^{\mathrm{ink}} = V_i^{\mathrm{cink}} - V_{i-1}^{\mathrm{cink}} \quad (3)$$

$$\eta_i = V_i^{\mathrm{th}} / \left(V_i^{\mathrm{th}} + V_i^{\mathrm{ink}}\right) \quad (4)$$

By IEC-MIP measurements, the distribution of connectivity η_i as a function of pore diameter d_i can be determined for all the paste mixtures as shown in Table 1. For a comparison, the standard MIP tests (including the first complete pressurization and depressurization) [26] and the 2nd intrusion (the second complete pressurization) [22] were performed as well. Both are illustrated in Fig. 3b. The 2nd intrusion follows the same procedure as for the first complete pressurization, but that no mercury entrapment occurs in the 2nd intrusion. The overall connectivity η_{p}, estimated from standard MIP, is expressed as the ratio of the effective porosity ϕ_{e} over the total open porosity ϕ_{t}, as shown in Eq. (5). The details for ϕ_{e}-value and ϕ_{t}-value can be referred to the pore size distribution results given in Fig. 3b.

$$\eta_{\mathrm{p}} = \left(\phi_{\mathrm{e}} / \phi_{\mathrm{t}}\right) \times 100\% \quad (5)$$

Compared to the overall connectivity η_{p}, the distribution of connectivity as a function of pore diameter (η_i vs. d_i) derived from the IEC-MIP tests enables to understand the pore connectivity at different scales, and will be more useful for studies of mass transport in cementitious materials. The IEC-MIP tests used in this work were composed of 20 intrusion-extrusion cycles. More cycles can be implemented to get a clearer picture of the pore connectivity. The measurement capacity of the apparatus was 420 MPa, while the maximum applied pressure was limited to 210 MPa (corresponding to the minimum intrusion pore diameter of 7 nm) to avoid severe cracking.

2.3. Chloride transport by rapid chloride migration test

Chloride ions transport occurs in a saturated cementitious material via its pore structure. Part of the chlorides will interact with pore walls. The interaction between chlorides and pore walls can be physical (chloride binding by surface forces on the pore walls) and/or chemical (chloride binding due to reaction with aluminate phases) [39]. Rapid chloride migration (RCM) as described in the guideline NT Build 492 [40] is an accelerated measurement. At the penetration

front, where the free-chloride concentration is low, the binding of chlorides is very low [41]. The obtained D_{RCM}-value, which indicates the migration coefficient at the front, is largely dependent on the pore structure of the specimen tested. The D_{RCM} is often called chloride migration coefficient in order to differentiate it from that obtained by immersion tests, e.g. NT Build 443 [42] or ASTM C1556–03 [43].

Three mortar specimens (ϕ100×50 mm) of each mixture were conducted with vacuum-saturation before they were used for the RCM tests. Chloride ions were penetrated rapidly in the mortar specimens under externally applied electric field. After a certain period of test, e.g. 24 hours, the mortar specimen was split and then sprayed with 0.1 mol·dm^{-3} $AgNO_3$ solution. The chloride penetration depths corresponding to the white deposits of AgCl were measured. The non-steady-state migration coefficient D_{RCM} ($\times 10^{-12}$ m^2/s) was calculated by the formula proposed by Tang and Nilsson [44], as:

$$D_{\mathrm{RCM}} = \frac{0.0239(237+T)L}{(U-2)t}\left(x_{\mathrm{d}} - 0.0238\sqrt{\frac{(237+T)Lx_{\mathrm{d}}}{U-2}}\right) \quad (6)$$

where T [˚C] is the average value of the initial and final temperatures in the anolyte solution; L [mm] is the thickness of the specimen; U [V] is the absolute value of the applied voltage; t [hour] is the test duration; x_d [mm] is the average value of the penetration depths.

3. Results

3.1. Pore connectivity

3.1.1 Overall connectivity η_p

The overall connectivity η_p of the paste mixtures shown in Table 1 was determined by the standard MIP tests. The results are presented in Table 2. A general trend is observed that the η_p-value decreases with age, particularly in the first 105 days. The addition of slag (MB4, MB5 and MB6) considerably decreases the η_p-value, compared with the reference OPC mixtures (M4, M5 and M6) at all ages. The fly ash-blended mixture MF5 has obviously higher η_p than the slag-blended mixture MB5, but shows tremendously lower η_p than the reference OPC mixture M5 at 370 days. In the presence of limestone powder LP, the ternary mixture MBL5 (or MFL5) exhibits substantially higher η_p than the LP-free binary mixture MB5 (or MF5). The capability of different blends in reducing η_p presents a descending order as slag, fly ash and limestone powder.

Table 2. Overall connectivity η_p of paste mixtures obtained by standard MIP tests.

3.1.2 Distribution of connectivity η_i for OPC binders

The distribution of connectivity η_i as a function of pore diameter d_i was determined by the IEC-MIP measurements and using Eqs. (2), (3) and (4). The result of the η_i-d_i plots for OPC paste mixture M4 at 28 days, as a representative, is displayed in Fig. 4. To better understand the η_i-d_i relationship, the pore size distribution from standard MIP test is given as well. There is a main peak corresponding to the most frequently occurring pore size, namely critical pore diameter d_{cr}. The connectivity η_i is strongly pore size-dependent, and can simply be divided into two categories according to the pores above or below the critical pore diameter d_{cr} (Fig. 4). For each category the change of η_i value is limited, but there is an abruptly drastic drop of the η_i value from the pores below d_{cr} ($\eta \approx 0.75$) to the pores above d_{cr} ($\eta \approx 0.35$).

In cementitious materials the large pores (diameter $d > d_{cr}$) are poorly connected and they can be connected normally through the small pores present in the contact area (see Fig. 1a). In the early stage of mercury penetration, significant mercury entrapment (ink-bottle effect) is expected, as evidently reflected by the low connectivity η_i values at $d > d_{cr}$ (Fig. 4). When the applied pressure corresponding to the critical pores is applied, a percolating network can be formed among the small pores present in the contact area. Concurrently, nearly all the large pores are filled with mercury. In this sense, the critical pore diameter d_{cr} represents the maximum continuous pore size, at which the mercury penetrates the bulk specimen. A further increase of the pressure results in the mercury to fill the pores below d_{cr}, and the associated ink-bottle pores belong to the small pores ($d < d_{cr}$), leading to low mercury entrapment and high connectivity, as demonstrated by the high η_i values at $d < d_{cr}$ (Fig. 4).

Figure 4. Two categories of the η_i-d_i plots in OPC paste (by IEC-MIP), according to the pore diameter d_i above or below the critical pore diameter d_{cr}, and pore size distribution of the OPC paste (by standard MIP).

Fig. 5 shows the η_i-d_i plots for OPC pastes cured under sealed condition from 28 to 370 days. All the curves are present in similar pattern. Regardless of the age, two groups (I and II) of

274 the η_i-d_i plots are found, which are separated by the critical pore diameters d_{cr} in the respective
275 mixtures. There is a sharp decrease in the connectivity η_i value from group I to group II. A
276 higher age from 28 to 370 days results in a larger ink-bottle effect, reflected by the lower
277 connectivity η_i in the wide pore size range. This is reasonable against the background of the
278 microstructural formation. As the progress of cement hydration, the hydration products (C-S-H
279 and calcium hydroxide) are continuously precipitated. The microstructure becomes denser and
280 the contact area (Fig. 1a) is enlarged so that connectivity η_i of the large pores ($d > d_{cr}$) is even
281 lower. The increased amount of hydrates C-S-H can entrap more small pores, leading to a lower
282 connectivity η_i at $d < d_{cr}$.
283

284 Figure 5. η_i-d_i relationship of OPC paste from 28 to 370 days determined by IEC-MIP tests.

285

286 With a higher age from 28 to 370 days, changes of the connectivity η_i of large pores (group
287 II) are limited while the connectivity η_i of small pores (group I) shows a relatively larger
288 change. It is well known that the moisture tends to occupy or moves toward to the smaller pore
289 size in the specimen by following the Kelvin law [45,46]. For specimens under sealed curing
290 condition, the small pores are considered filled with water while the large pores are filled with
291 gas. The newly formed products from cement hydration beyond 28 days are more readily to
292 precipitate in the (water-filled) small pores, rather than in the (gas-filled) large pores. As a
293 consequence, the packing density of hydrates is higher and the connectivity of the small pores
294 (inside the clusters of hydrates) becomes lower. A similar finding has been reported previously
295 by Mehta and Manmohan [47], who studied the evolution of microstructure with age and found
296 that at early stage the hydration products were formed in large capillary pores, whereas later on
297 in small capillary pores.
298 From the results in Figs. 4 and 5, it is concluded that the pores above critical pore diameter
299 d_{cr} cannot make up a connected network for mass transport while below the d_{cr} the pores can
300 form interconnected paths allowing mass transport. The small capillary pores in cementitious
301 materials are not randomly distributed in its entirely, but do impose the following principles:
302 1) The small capillary pores (above d_{cr}) are highly connected with the large capillary pores.
303 2) The small capillary pores (below d_{cr}) are mutually interconnected, and they have little
304 connection with the large capillary pores. These small capillary pores can make up a
305 percolating pore network for mass transport in the cementitious materials.

306 3.1.3 Distribution of connectivity η_i for blended binders

307 Fig. 6 summarizes the η_i-d_i relationship in the paste specimens made with blended binders
308 cured after 370 days. As indicated, the conductivity η_i is not so much different for the large
309 capillary pore group (diameter d > 0.05 μm) and mostly lies in a *narrow* range of 22~35%,
310 regardless of the binder type. For small capillary pore group (d < 0.05 μm), however, the η_i
311 value differs significantly in the wide range of 18~80%, depending on the type of binder used.
312 The inclusion of SCMs, either FA or BFS, results in substantially lower connectivity η_i of small
313 capillary pores. Besides cement hydration, additional pozzolanic or chemical reactions can take
314 place in the presence of FA or BFS. C-S-H gels and/or other chemical compounds are produced.
315 Subsequently, plenty of small capillary pores can be segmented or clogged, resulting in lower
316 connectivity of the small capillary pores. The connectivity of the fine pores (< 0.02 μm) is
317 considerably lower in BFS-blended binder MB5 than in FA-blended binder MF5. It is a result of
318 the higher chemical reactivity of BFS than FA. The addition of LP, in contrast, obviously
319 increases the connectivity η_i of small capillary pores in view of the η_i-d_i plots between MF5
320 and MFL5. This results from the dilution effect of LP and thereby the microstructure is
321 coarsened.

322 A conclusion can be arrived at that the addition of SCMs primarily results in the
323 reconstruction of small capillary pores in the cementitious materials. This is of particular interest
324 so far as the mass transport is concerned. The capability in reducing the pore connectivity
325 presents an ascending order in the binders as LP < FA < BFS.

326

327 Figure 6. Effect of binder type on the η_i-d_i relationship in paste specimens (w/b = 0.5, 370
328 days) determined by IEC-MIP tests.

329

330 *3.2. Chloride migration coefficient D_{RCM}*

331 The chloride migration coefficient D_{RCM} of mortar specimens was measured following the
332 rapid migration test method. Fig. 7a presents the results of D_{RCM} for OPC and FA-blended
333 binders. Between 28 days and 2 years, the D_{RCM} value shows a generally decreasing trend. For
334 OPC binders a slight increase in the D_{RCM} value can be seen at around 1 year. This is attributable
335 to the delayed ettringite formation, triggered as a result of alkali leaching out of the mortar
336 specimens under moist curing circumstances [19,48]. Alkali leaching can lead to reduced pH,

337 which is favorable for ettringite precipitation. The sulfate adsorbed in the C-S-H gel can also be
338 desorbed owing to the reduced pH [49]. The D_{RCM} value again shows a decreasing trend after 2
339 year, but that a gradual decrease can be expected. For FA-blended binders, the D_{RCM} value at 28
340 days is much higher than that in the neat OPC binders. However, the D_{RCM} value decreases
341 significantly from 28 to 105 days. A relatively slow decrease of the D_{RCM} value is followed after
342 105 days. With the addition of limestone powder (LP) the ternary binder MFL5 has a slightly
343 lower D_{RCM} than the LP-free binary binder MF5.
344 Fig. 7b shows the chloride migration coefficient D_{RCM} in the BFS-blended binders. The
345 D_{RCM} value decreases with age, an expected observation. A pronounced effect of the w/b (0.4,
346 0.5 and 0.6) on the D_{RCM} value is found at 28 days. Such effect is, however, diminished in view
347 of the D_{RCM} values for binders MB4, MB5 and MB6 after 105 days. This points to a reasonable
348 consideration that the overall connectivity η_p, differing greatly between MB4, MB5 and MB6
349 as given in Table 2, is inappropriate to indicate the chloride transport property of BFS-blended
350 binders. Compared to MB5, further incorporation of LP (MBL5) results in an obvious decrease
351 of the D_{RCM} value in the entire age. Upon closer observation, it is found that the D_{RCM} values of
352 the BFS-blended binder MB5 are substantially lower than those of the OPC binder M5 but appear
353 to be similar to those of the FA-blended binder MF5.
354

355 Figure 7. Changes of chloride migration coefficient D_{RCM} with age: (a) OPC and FA-blended
356 mortars; (b) BFS-blended mortars.

357

358 *3.3. Chloride migration coefficient D_{RCM} vs. overall connectivity η_p*

359 The roles of the factors including w/b, age and SCMs in the chloride migration coefficient
360 D_{RCM} are primarily the result of their effects on the pore connectivity characteristics. The overall
361 connectivity η_p, a conventionally adopted parameter, has been determined based on standard
362 MIP tests and using Eq. (5). Fig. 8 depicts the chloride migration coefficient D_{RCM} against the
363 overall connectivity η_p for all the mixtures given in Table 1. The D_{RCM} values are taken from
364 Fig. 7 and the η_p values from Table 2. The specimens are 28, 105, 182 and 370 days old. All
365 D_{RCM} *vs.* η_p plots, except two (PF5 and PFL5 at 28 days), can be categorized into two groups.
366 One group is for the specimens with OPC binders, where the D_{RCM}-value increases markedly
367 with an increase of the overall connectivity η_p. The other group is for the specimens with

368 blended binders, where the change of D_{RCM}-value is limited when the overall connectivity η_p
369 increases from around 25% to 58%. A general D_{RCM}-η_p relationship covering all the binders
370 cannot be obtained.
371

372 Figure 8. Two-group relationship between chloride migration coefficient D_{RCM} and overall
373 connectivity η_p for OPC and blended mortars (28~370 days old).

374

375 It can be inferred that the often-adopted concept of overall connectivity η_p is suitable to
376 predict the chloride transport property in saturated OPC mortars while, surprisingly, it is not
377 effective in judging the chloride transport property in saturated blended mortars. A discussion
378 on this point follows below.

379 **4. Discussion**

380 *4.1. Dependence of chloride transport on pore connectivity*

381 4.1.1 Pore structure and transport property: role of small capillary pores

382 To understand the pore structure-related transport property in saturated porous systems, one
383 needs to clarify two issues: (i) the pores all over the microstructure need to be subdivided into
384 *one part* that contributes to ionic transport and *another part* that does not; (ii) the connectivity
385 of the pores that contribute to ionic transport needs to be determined.
386 Fig. 9 shows a sketch of the microstructure in hydrated cementitious systems. Fig. 10
387 illustrates the typical pore size distribution curve from standard MIP tests. A choke point
388 corresponding to the threshold pore diameter d_{th} can be observed. The large capillary pores above
389 d_{th} show a flat pattern, while there is a steep change for small capillary pores below d_{th} (Fig. 10).
390 Transport of chloride ions in the large capillary pores can hardly take place until the chloride
391 ions have penetrated a long percolative chain of intermediate small capillary pores. Different
392 contributions of various pore categories to chloride transport can be described as follows.
393 1) The large capillary pores (I: $d_{th} < d \leq 10$ μm) are mostly disconnected and have minor
394 influence on the ionic transport property. A higher volume of the large capillary pores will
395 result in a higher total porosity, as well as a higher ink-bottle porosity (a lower effective
396 porosity) and a lower overall connectivity η_p (Eq. (5)), but will not significantly affect the

rate of ionic transport. For determinations of the threshold pore diameter d_{th} reference can be made to the tangent method provided by Liu and Winslow [50].

2) The small capillary pores (II: 0.01 μm < $d \leq d_{th}$) play a major role in the rate of ionic transport. The connectivity of small capillary pores and its relation to ionic transport will be quantitatively described in Subsections 4.1.2 and 4.1.3.
3) Ionic transport in the gel pores (III: $d \leq 0.01$ μm) is so slow that it is negligible [51,52], compared to ionic transport in the capillary pores in range II.

Figure 9. A sketch of the microstructure in hydrated cementitious systems.

Figure 10. Three pore categories based on MIP-derived pore size distribution. d_{th} - threshold pore diameter.

4.1.2 Connectivity of small capillary pores (0.01 μm < $d \leq d_{th}$)

Two types of pore geometry of *small* capillary pores (0.01 μm < $d \leq d_{th}$, range II of Fig. 10) can be distinguished: throat type (volume V_{sc}^{th}) and ink-bottle type (volume V_{sc}^{ink}). The connectivity of small capillary pores in range II, η_{sc}, is expressed as:

$$\eta_{sc} = V_{sc}^{th}/(V_{sc}^{th} + V_{sc}^{ink}) \quad (7)$$

The η_{sc}-value of each specimen can be determined based on IEC-MIP tests. To understand the volume V_{sc}^{ink} of small capillary *ink-bottle* pores, differentiation between *small* capillary ink-bottle pores and *large* capillary ink-bottle pores is required. This can be achieved by studying the distribution of connectivity η as a function of pore diameter *d*. Fig. 11 shows an example of the η-*d* plots measured from the IEC-MIP tests.

1) At $d_{cr} \leq d \leq d_{th}$, mercury penetrates into both small capillary (throat and ink-bottle) pores and large capillary (ink-bottle) pores (Fig. 9). The ink-bottle effect is large, corresponding to low connectivity value ($\eta \approx 0.35$) (Fig. 11).
2) At 0.01 μm < $d \leq d_{s,cr}$, mercury only penetrates into small capillary pores (Fig. 9), including *throat* type and *ink-bottle* type, resulting in small ink-bottle effect and high connectivity

value ($\eta \approx 0.75$) (Fig. 11). The $d_{s,cr}$ is the pore size smaller than, but close to, the critical pore diameter d_{cr}.

It is not easy to obtain the V_{sc}^{ink}-value directly from mercury intrusion-extrusion cycles at pore size range II (0.01 μm < $d \leq d_{th}$). However, given that the connectivity η value is almost the same for small capillary pores in the range 0.01 μm < $d \leq d_{s,cr}$, it is reasonable to consider that the connectivity η_{sc} of small capillary pores in range II (0.01 μm < $d \leq d_{th}$) is equal to the connectivity $\eta_{s,cr}$ of pores (0.01 μm < $d \leq d_{s,cr}$). The $\eta_{s,cr}$-value is obtainable from mercury intrusion-extrusion cycles at pore size range 0.01 μm < $d \leq d_{s,cr}$, and can be expressed as Eq. (8).

$$\eta_{sc} = \eta_{s,cr} = \frac{V_s^{th}}{V_s^{in}} \times 100\% \quad (8)$$

where V_s^{th} and V_s^{in} are the cumulative throat pore volume and the cumulative intrusion volume, respectively, when mercury intrudes the pores with diameters from $d_{s,cr}$ to 0.01 μm. The V_s^{th}-value can be determined from the pore size distribution obtained by the 2nd pressurization, i.e. the 2nd intrusion as illustrated in Fig. 3b. The V_s^{in}-value can be determined from the pore size distribution obtained by the 1st pressurization, i.e. 1st intrusion as illustrated in Fig. 3b. Determinations of both V_s^{th}-value and V_s^{in}-value are illustrated in Fig. 11.

Figure 11. Determination of the connectivity η_{sc} of small capillary pores (range II: 0.01 μm < $d \leq d_{th}$) in cement paste (w/b = 0.4, 28-day-old). d_{th} – threshold pore diameter; d_{cr} – critical pore diameter; $d_{s,cr}$ is the pore diameter smaller than, but close to, the critical pore diameter d_{cr}.

4.1.3 Relationship between chloride migration coefficient and connectivity of small capillary pores

The connectivity η_{sc} of small capillary pores (range II: 0.01 μm < $d \leq d_{th}$) has been determined with Eq. (8) for various mixtures. By replacing the overall connectivity η_p with the connectivity η_{sc} of small capillary pores, the D_{RCM}-η_p plots shown in Fig. 8 are then transformed into the D_{RCM}-η_{sc} plots, as shown in Fig. 12a. For a given mixture the η_{sc} value is generally higher than the η_p value. A power equation, as formulated in Eq. (9), is found to well describe the D_{RCM}-η_{sc} relationship covering the plots of all OPC and blended binders. The exponent of 4 suggests that the chloride transport property in saturated mortars significantly

452 depends on the connectivity η_{sc} of small capillary pores. Fig. 12b gives the relationship between
453 logD_{RCM} and η_{sc} in logarithmic plots. The dependence of chloride ions transport on the η_{sc} is
454 highlighted accordingly. Based on the results given in Fig. 12a, it is clear that compared to the
455 conventional concept of overall connectivity η_p (calculated by Eq. (5)), the connectivity η_{sc} of
456 small capillary pores (calculated by Eq. (8)) is a better parameter for indicating the ionic transport
457 in saturated cementitious materials irrespective of the binder type.

$$D_{RCM} = 46.86 \cdot (\eta_{sc})^4 \quad (9)$$

458

459 Figure 12. (a) Power relationship between chloride migration coefficient D_{RCM} and
460 connectivity η_{sc} of small capillary pores (0.01 μm < $d \leq d_{th}$), regardless of the binders (OPC
461 and blends); (b) Relationship between logD_{RCM} and η_{sc} in logarithmic plots.

462

463 *4.2 Examination of isolated pores*

464 Mercury penetration can measure the open porosity, including continuous pores and dead-
465 end (ink-bottle) pores, but that the isolated pores cannot be filled with mercury. A brief
466 discussion on the presence of isolated pores in OPC pastes is provided below.
467 From the reports by Neville [53] and Wong and Buenfeld [54], the total shrinkage of
468 hardened OPC pastes is very small in comparison to the porosity obtained by mercury
469 porosimetry. The reduction of porosity with age originates from continuous precipitation of
470 hydration products. In some cases, the hydration products are densely packed and isolated pores
471 can be formed inside the clusters of hydration products. Volume transformations of capillary
472 water to the chemically bound water, as well as to the gel water, account for a main part of the
473 pore volume reduction in hydrating cement paste. The different types of water phase in cement
474 paste are illustrated in Fig. 13. Capillary water is the water held in capillary pores. Part of the
475 capillary water is physically adsorbed on the pore walls. The adsorbed capillary water is hardly
476 available for cement hydration. The free capillary water, in contrast, can easily be mobilized for
477 cement hydration. Gel water, also termed interlayer water, refers to the water between C-S-H gel
478 layers. For complete hydration of the cement, the non-evaporable water amounts to 0.22~0.25
479 g/g of the anhydrous cement [5].
480

Figure 13. Illustration of water phases in the cement paste [55].

Cement grains react with the free capillary water resulting in a net reduction of the total volume of water and solid. The capillary water (specific volume = 1 cm^3/g) can be partly transformed into chemically bound water (specific volume = 0.72 cm^3/g) [56]. Subsequently, the originally water filled space (i.e. initial porosity ϕ_0) is gradually occupied by solid phases. Reaction of 1 g capillary water into chemically bound water can result in a reduction of the pore volume of 0.72 cm^3. In accordance to Powers' model [55], 1 g reacted cement products contain around 0.19 g gel water. The gel water is highly compressed, with a specific volume of 0.9 cm^3/g [56]. For the same amount of water by weight, the volume of gel water is less than that of capillary water by around 10%.

The presence of isolated pores can be analyzed roughly by tracing changes of the total open porosity ϕ_t with cement hydration. The initial porosity ϕ_0 (age t = 0), with the air voids not considered, can be computed as:

$$\phi_0 = \frac{w/b}{w/b + m_b/\rho_b + m_c/\rho_c} \tag{10}$$

where w/b is the water-binder-ratio; m_c and m_b are the mass percentage of Portland cement and blended cement, respectively; ρ_c and ρ_b are the specific gravity of Portland cement and blended cement, respectively. For pure Portland cement pastes, $m_b = 0$.

Table 3 shows the initial porosity ϕ_0 of various paste mixtures calculated with Eq. (10). The w/b greatly influences the initial porosity ϕ_0. Increasing 0.1 of the w/b results in the initial porosity ϕ_0 to increase by about 5%.

Table 3. Initial porosity ϕ_0 of paste specimens according to Eq. (10).

Changes of the total open porosity ϕ_t with hydration period t, $\Delta\phi(t) = \phi_0 - \phi_t$, were determined, with the ϕ_t value obtained from mercury porosimetry measurements. Fig. 14 shows the evolution of the $\Delta\phi(t)$ value with age for OPC and BFS-blended pastes with w/b of 0.4, 0.5 and 0.6. As expected, a rise trend in the $\Delta\phi(t)$ value is observed for a higher age. This is attributed to the continuous precipitation of hydration products. Of particular interest to note is that the $\Delta\phi(t)$ value is higher in the OPC paste with low w/b = 0.4 (M4) than that with high

w/b (M6) at all ages. Precipitation of solid hydrates and formation of isolated pores are the two main reasons leading to changes of the $\Delta\phi(t)$ value. It is well known that increasing the w/b can accelerate the cement hydration and more hydration products will be created [57,58]. Then the higher $\Delta\phi(t)$ value in M4 should be most possibly owing to the fact that more isolated pores have been formed in M4 than in M6, assuming that other conditions are the same between the two. These isolated pores were not included in the total open porosity ϕ_t as measured by mercury porosimetry. The similar finding holds also for the BFS-blended pastes. In the first 182 days, the $\Delta\phi(t)$ values are obviously higher in MB4 (BFS, w/b = 0.4) than those in MB5 (BFS, w/b = 0.5) and MB6 (BFS, w/b = 0.6).

As analyzed above, more isolated pores are formed in the mixtures with low w/b of 0.4. At 28 days, the $\Delta\phi(t)$ value is 1.9% larger in M4 than in M6, suggesting that the porosity of isolated pores should be at least 1.9% for OPC paste M4 (w/b = 0.4). Likewise, the porosity of isolated pores is calculated to be at least 4.1% for BFS-blended paste MB4 (w/b = 0.4) at 28 days. The BFS reacts with the calcium hydroxide and transforms into the secondary C-S-H, whereby more small pores can be entrapped and turn into isolated pores. This may be the reason for the higher volume of isolated pores in MB4 than in M4.

Figure 14. Open porosity change ($\Delta\phi(t) = \phi_0 - \phi_t$) with age for OPC and BFS-blended pastes with w/b of 0.4, 0.5 and 0.6. ϕ_0 is the initial porosity according to Eq. (10) and ϕ_t is the total open porosity by mercury porosimetry measurements.

5. Conclusions

An innovative measurement, i.e. *intrusion-extrusion cyclic mercury porosimetry* (IEC-MIP), has been introduced. Compared to standard MIP tests, the IEC-MIP tests enable to obtain a much clearer picture of the pore connectivity at different scales and provide evident basis for studies of mass transport in saturated cementitious materials as estimated by rapid chloride migration tests. According to experimental studies of this work, the key findings are outlined as follows.

1) The connectivity η of the pores in cementitious materials strongly depends on the pore diameter d. For OPC binders, an abruptly drastic drop of the connectivity η is found from small pore group (d < critical pore diameter d_{cr}) to large pore group ($d > d_{cr}$).

2) For OPC binders the small capillary pores are highly interconnected and mostly present as continuous pores. Incorporation of supplementary cementitious materials results in a significant reconstruction of the small capillary pores. The connectivity of the pores below 0.05 μm is substantially decreased by the addition of slag or fly ash while increased by including limestone powder.
3) For OPC binders a higher overall connectivity η_{p} leads to a higher chloride migration coefficient D_{RCM}. This finding, however, does not hold for binders blended with fly ash or slag.
4) A novel transport parameter, *connectivity* η_{sc} *of small capillary pores* (0.01 μm < $d \leq$ threshold pore diameter d_{th}), is put forward. A power D_{RCM}-η_{sc} relationship is established covering all the binders (OPC, slag, fly ash and limestone powder).

Acknowledgments

The authors wish to acknowledge the assistant provided by technicians in the Microlab, Delft University of Technology (TU Delft), The Netherlands. A special appreciation goes to Prof. Klaas van Breugel (TU Delft) for the valuable suggestions. The work was supported by the Talent-Introduction Program of Fuzhou University (Grant No. GXRC-19023).

Conflicts of Interest

The authors declare no conflict of interest.

References

[1] J. Stark, Recent advances in the field of cement hydration and microstructure analysis, Cem. Concr. Res. 41 (2011) 666–678.
[2] P. Zhang, F.H. Wittmann, P. Lura, H.S. Mueller, S. Han, T. Zhao, Application of neutron imaging to investigate fundamental aspects of durability of cement-based materials: A review, Cem. Concr. Res. 108 (2018) 152–166.
[3] H.M. Jennings, Refinements to colloid model of C-S-H in cement: CM-II, Cem. Concr. Res. 38 (2008) 275–289.
[4] T.C. Powers, T.L. Brownyard, Studies of the physical properties of hardened Portland cement paste. Part 2. Studies of water fixation, J. Am. Concr. Inst. 18 (1946) 249–303.

572 [5] K. van Breugel, Numerical simulation of hydration and microstructural development in
573 hardening cement-based materials, PhD thesis, Delft University of Technology, The
574 Netherlands, 1991.
575 [6] D.P. Bentz, Fibers, percolation, and spalling of high performance concrete, ACI Mater. J.
576 97 (2000) 351–359.
577 [7] P. Navi, C. Pignat, Simulation of cement hydration and the connectivity of the capillary
578 pore space, Adv. Cem. Based Mater. 4 (1996) 58–67.
579 [8] D.P. Bentz, E.J. Garboczi, Percolation of phases in a three-dimensional cement paste
580 microstructural model, Cem. Concr. Res. 21 (1991) 325–344.
581 [9] G. Ye, X. Liu, G. de Schutter, L. Taerwe, P. Vandevelde, Phase distribution and
582 microstructural changes of self-compacting cement paste at elevated temperature, Cem.
583 Concr. Res. 37 (2007) 978–987.
584 [10] P. Stroeven, J. Hu, D.A. Koleva, Concrete porosimetry: Aspects of feasibility, reliability
585 and economy, Cem. Concr. Compos. 32 (2010) 291–299.
586 [11] G. Sant, D.P. Bentz, J. Weiss, Capillary porosity depercolation in cement-based materials:
587 measurement techniques and factors which influence their interpretation, Cem. Concr. Res.
588 41 (2011) 854–864.
589 [12] N. Bossa, P. Chaurand, J. Vicente, D. Borschneck, C. Levard, O. A.C.J. Rose, Micro- and
590 nano-X-ray computed-tomography: a step forward in the characterization of the pore
591 network of a leached cement paste, Cem. Concr. Res. 67 (2015) 138–147.
592 [13] R. He, H. Ma, R.B. Hafiz, C. Fu, X. Jin, J. He, Determining porosity and pore network
593 connectivity of cement-based materials by a modified non-contact electrical resistivity
594 measurement: Experiment and theory, Mater. Des. 156 (2018) 82–92.
595 [14] M.H.N. Yio, H.S. Wong, N.R. Buenfeld, 3D pore structure and mass transport properties of
596 blended cementitious materials, Cem. Concr. Res. 117 (2019) 23–37.
597 [15] G.E. Archie, The electrical resistivity log as an aid in determining some reservoir
598 characteristics, Trans. AIME 146 (1942) 54–62.
599 [16] S. Whitaker, Flow in porous media I: A theoretical derivation of Darcy’s law, Transport
600 Porous Med. 1 (1) (1986) 3–25.
601 [17] X. Zhang, X. Zhang, H. Taira, H. Liu, Error of Darcy's law for serpentine flow fields:
602 Dimensional analysis, J. Power Sources 412 (2019) 391–397.
603 [18] P.W.J. Glover, M.J. Hole, J. Pous, A modified Archie’s law for two conducting phases,
604 Earth Planet Sc. Lett. 180 (2000) 369–383.

[19] Y. Zhang, Non-saturated chloride diffusion in sustainable cementitious materials, PhD thesis, Delft University of Technology, The Netherlands, 2018.

[20] D.P. Bentz, CEMHYD3D: A Three-Dimensional Cement Hydration and Microstructure Development Modelling Package. Version 2.0 NISTIR 6485, U.S. Department of Commerce, Washington, DC., 1997.

[21] C. Liu, G. Liu, Z. Liu, L. Yang, M. Zhang, Y. Zhang, Numerical simulation of the effect of cement particle shapes on capillary pore structures in hardened cement pastes, Constr. Build. Mater. 173 (2018) 615–628.

[22] G. Ye, Experimental study and numerical simulation of the development of the microstructure and permeability of cementitious materials, PhD Thesis, Delft University of Technology, The Netherlands, 2003.

[23] M. Zhang, K. Xu, Y. He, A.P. Jivkov, Pore-scale modelling of 3D moisture distribution and critical saturation in cementitious materials, Constr. Build. Mater. 64 (2014) 222–230.

[24] K.K. Aligizaki, Pore structure of cement-based materials: Testing, interpretation and requirements, CRC Press, 2006.

[25] Y. Zhang, B. Yang, Z.X. Yang, G. Ye, Ink-bottle effect and pore size distribution of cementitious materials identified by pressurization–depressurization cycling mercury intrusion porosimetry, Mater. 12 (9) (2019):1454.

[26] S. Diamond, Mercury porosimetry: an in appropriate method for the measurement of pore size distributions in cement-based materials, Cem. Concr. Res. 30 (10) (2000) 1517–1525.

[27] E.J. Garboczi, Permeability, diffusivity and microstructural parameters: A critical review, Cem. Concr. Res. 20 (1990) 591–601.

[28] M.A.B. Promentilla, T. Sugiyama, T. Hitomi, N. Takeda, Quantification of tortuosity in hardened cement pastes using synchrotron-based X-ray computed microtomography, Cem. Concr. Res. 39 (2009) 548–557.

[29] X. Sun, Q. Dai, K. Ng, Computational investigation of pore permeability and connectivity from transmission X-ray microscope images of a cement paste specimen, Constr. Build. Mater. 68 (2014) 240–251.

[30] S. Zhou, D. Liu, Y. Cai, Y. Yao, Z. Li, 3D characterization and quantitative evaluation of pore-fracture networks of two Chinese coals using FIB-SEM tomography, Int. J. Coal Geol. 174 (2017) 41–54.

[31] F. Gao, Y. Song, Z. Li, F Xiong, L. Chen, X. Zhang, Z. Chen, J. Moortgat, Quantitative characterization of pore connectivity using NMR and MIP: A case study of the Wangyinpu

638 and Guanyintang shales in the Xiuwu basin, Southern China. Int. J. Coal Geol. 197 (2018)
639 53–65.
640 [32] P. Zhang, F.H. Wittmann, M. Vogel, H.S. Müller, T. Zhao, Influence of freeze-thaw cycles
641 on capillary absorption and chloride penetration into concrete, Cem. Concr. Res. 100 (10)
642 (2017) 60–67.
643 [33] E. Kierlik, P.A. Monson, M.L. Rosinberg, L. Sarkisov, G. Tarjus, Capillary condensation
644 in disordered porous materials: Hysteresis versus equilibrium behavior, Phys. Rev. Lett.
645 2001, 87:055701.
646 [34] R. Valiullin, S. Naumov, P. Galvosas, J. Kärger, H.J. Woo, F. Porcheron, P.A. Monson,
647 Exploration of molecular dynamics during transient sorption of fluids in mesoporous
648 materials, Nature, 443 (2006) 965–968.
649 [35] Y. Zhang, G. Ye, Experimental study on pore connectivity and its influence on chloride
650 transport in saturated cementitious system, The 3rd International RILEM Conference on
651 Microstructure Related Durability of Cementitious Composites, 24-26 October 2016,
652 Nanjing, China, vol. 117, pp. 1–8.
653 [36] EN 196-1, Methods of testing cement, Determination of strength, 2005, ISBN: 0580456706.
654 [37] C. Galle, Effect of drying on cement-based materials pore structure as identified by mercury
655 intrusion porosimetry: A comparative study between oven-, vacuum-, and freeze-drying,
656 Cem. Concr. Res. 31 (2001) 1467–1477.
657 [38] E.W. Washburn, The dynamics of capillary flow, Phys. Rev. 17 (1921) 273–283.
658 [39] G.K. Glass, N.R. Buenfeld, The influence of chloride binding on the chloride induced
659 corrosion risk in reinforced concrete, Corros. Sci. 42 (2000) 329–344.
660 [40] NT Build 492, Concrete, Mortar and Cement-Based Repair Materials: Chloride Migration
661 Coefficient from Non-Steady-State, Migration Experiments, 1999.
662 [41] P. Spiesz, H.J.H. Brouwers, The apparent and effective chloride migration coefficients
663 obtained in migration tests, Cem. Concr. Res. 48 (2013) 116–127.
664 [42] NT Build 443, Concrete, Hardened: Accelerated Chloride Penetration, 1995.
665 [43] ASTM C1556–03, Standard Test Method for Determining the Apparent Chloride Diffusion
666 Coefficient of Cementitious Mixtures by Bulk Diffusion, 042003 (2016) 1–7.
667 [44] L.P. Tang, L-O. Nilsson, Rapid determination of the chloride diffusivity in concrete by
668 applying an electrical field, ACI mater. J. 89 (1) (1992) 49–53.
669 [45] Y. Zhang, X.W. Ouyang, Z.X. Yang, Microstructure-based relative humidity in
670 cementitious system due to self-desiccation, Mater. 2019, 12 (8):1214.

671 [46] Y. Zhang, M. Zhang, G. Ye, Influence of moisture condition on chloride diffusion in
672 partially saturated ordinary Portland cement mortar, Mater. Struct. 2018, 51:36.
673 [47] P.K. Mehta, D. Manmohan, Pore size distribution and permeability of hardened cement
674 pastes, Proc. the Seventh International Congress on the Chemistry of Cement, Paris, 3 (7)
675 (1980) 1–5.
676 [48] S. Diamond, The relevance of laboratory studies on delayed ettringite formation to DEF in
677 field concretes, Cem. Concr. Res. 30 (12) (2000) 1987–1991.
678 [49] L. Divet, R. Randriambololona, Delayed ettringite formation: The effect of temperature and
679 basicity on the interaction of sulfate and C-S-H phase, Cem. Concr. Res. 28 (1998) 357–
680 363.
681 [50] Z. Liu, D. Winslow, Sub-distributions of pore size: a new approach to correlate pore
682 structure with permeability, Cem. Concr. Res. 25 (4) (1995) 769–778.
683 [51] J.S. Mindess, J.F. Young, Concrete, Prentice-Hall, Englewood Cliffs, NJ, 1981.
684 [52] Y. Zhang, G. Ye, A model for predicting the relative chloride diffusion coefficient in
685 unsaturated cementitious materials, Cem. Concr. Res. 115 (2019) 133–144.
686 [53] A.M. Neville, Properties of Concrete (4th edn), Wiley, New York, 1995.
687 [54] H.S. Wong, N.R. Buenfeld, Determining the water–cement ratio, cement content, water
688 content and degree of hydration of hardened cement paste: Method development and
689 validation on paste samples, Cem. Concr. Res. 39 (2009) 957–965.
690 [55] T.C. Powers, Studies of the physical properties of hardened Portland cement paste, J. Amer.
691 Chem. Soc. 43 (1946) 101–132.
692 [56] H.J.H. Brouwers, The work of Powers and Brownyard revisited: Part 1, Cem. Concr. Res.
693 34 (2004) 1697–1716.
694 [57] S. Hanehara, F. Tomosawa, M. Kobayakawaa, K.R. Hwan, Effects of water/powder ratio,
695 mixing ratio of fly ash, and curing temperature on pozzolanic reaction of fly ash in cement
696 paste, Cem. Concr. Res. 31 (2001) 31–39.
697 [58] D.P. Bentz, Influence of water-to-cement ratio on hydration kinetics: Simple models based
698 on spatial considerations, Cem. Concr. Res. 36 (2) (2006) 238–244.

Figures

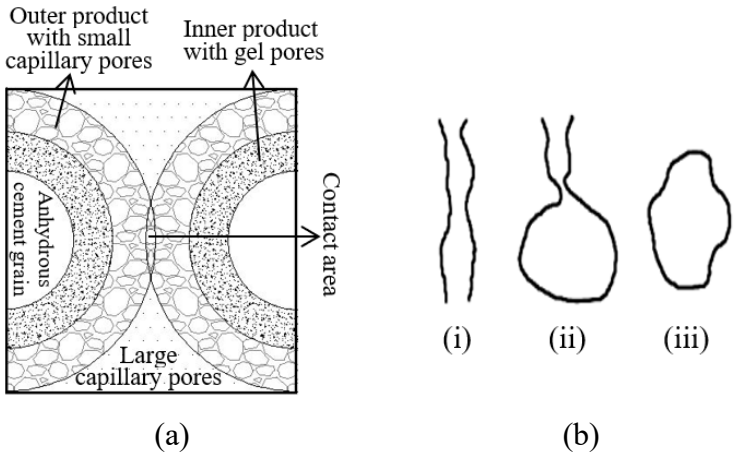

Figure 1. (a) Hydration cell of two cement grains; (b) Pore geometry for (i) continuous pore, (ii) dead-end (ink-bottle) pore and (iii) isolated pore.

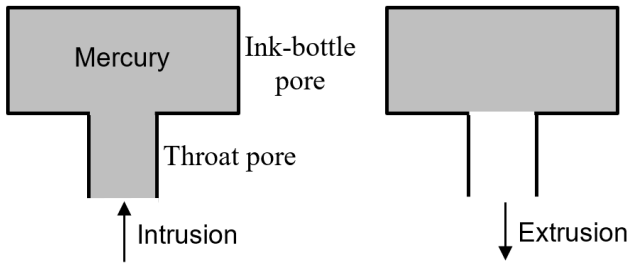

Figure 2. Mercury intrusion-extrusion hysteresis in a pore system with a throat pore connecting an ink-bottle pore.

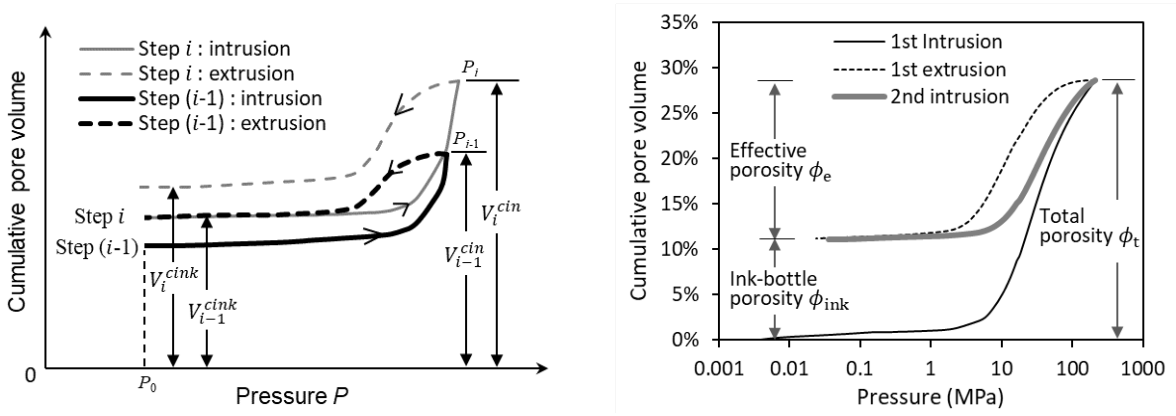

(a) (b)

711 Figure 3. (a) Test sequence of intrusion-extrusion cyclic mercury porosimetry (IEC-MIP): from
712 step (i-1) to step i, the cumulative intrusion volume increases from V_{i-1}^{cin} to V_i^{cin} and the
713 cumulative ink-bottle volume increases from V_{i-1}^{cink} to V_i^{cink}; (b) Standard mercury intrusion
714 porosimetry (MIP), consisting of an intrusion from the minimum to the maximum pressure and
715 an extrusion from the maximum to the minimum pressure, and the 2nd intrusion.

716

717

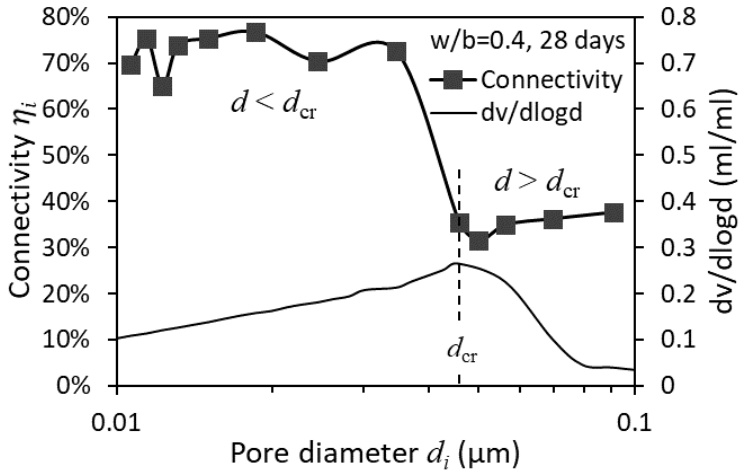

718

719 Figure 4. Two categories of the η_i-d_i plots in OPC paste (by IEC-MIP), according to the pore
720 diameter d_i above or below the critical pore diameter d_{cr}, and pore size distribution of the OPC
721 paste (by standard MIP).

722

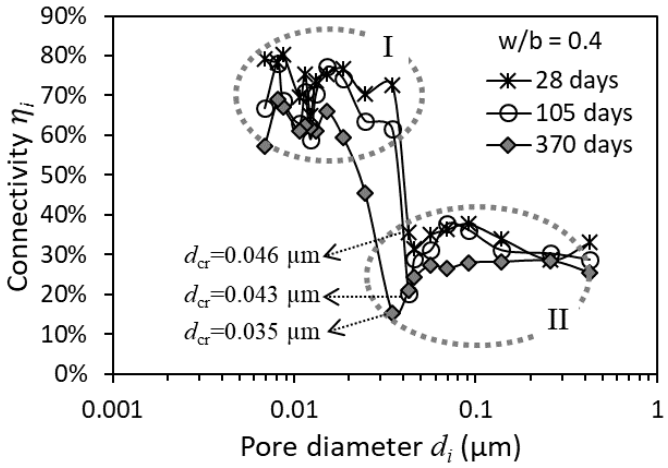

723

724 Figure 5. η_i-d_i relationship of OPC paste from 28 to 370 days determined by IEC-MIP tests.

725

726

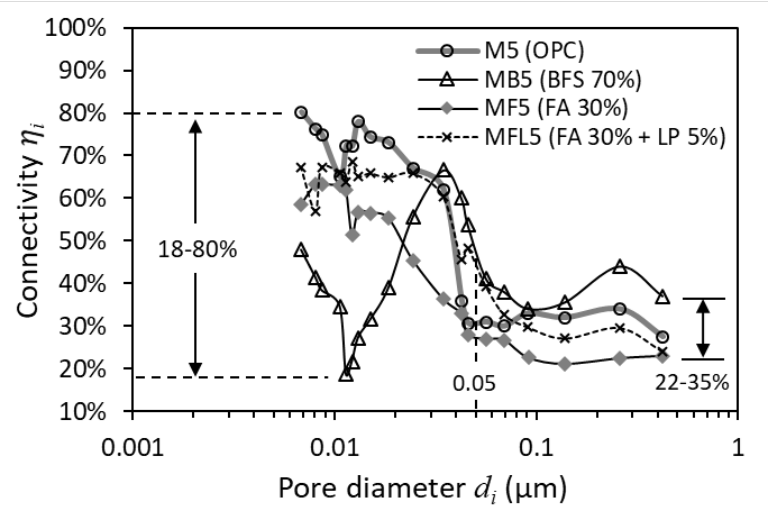

727

728 Figure 6. Effect of binder type on the η_i-d_i relationship in paste specimens (w/b = 0.5, 370
729 days) determined by IEC-MIP tests.

730

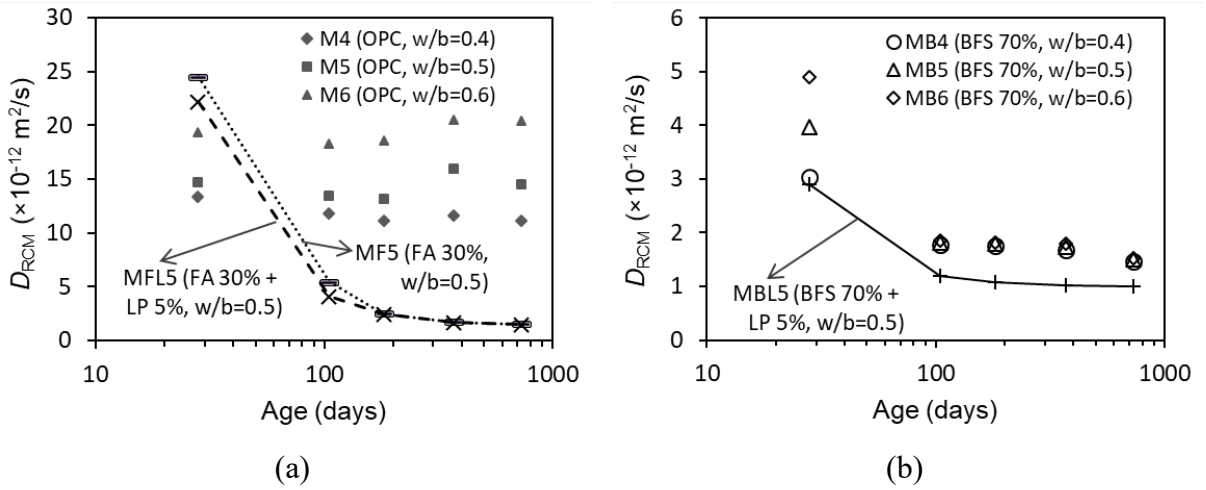

731 Figure 7. Changes of chloride migration coefficient D_{RCM} with age: (a) OPC and FA-blended
732 mortars; (b) BFS-blended mortars.

733

734

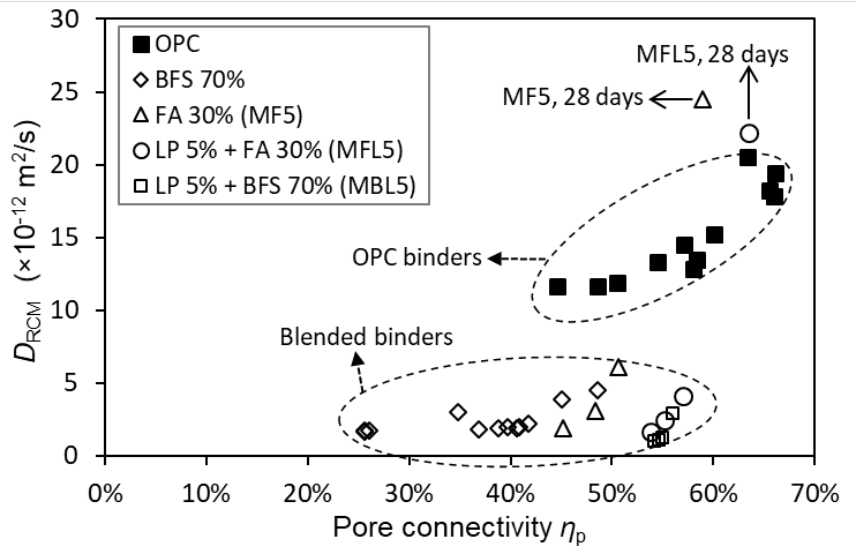

735

736 Figure 8. Two-group relationship between chloride migration coefficient D_{RCM} and overall
737 connectivity η_p for OPC and blended mortars (28~370 days old).

738

739

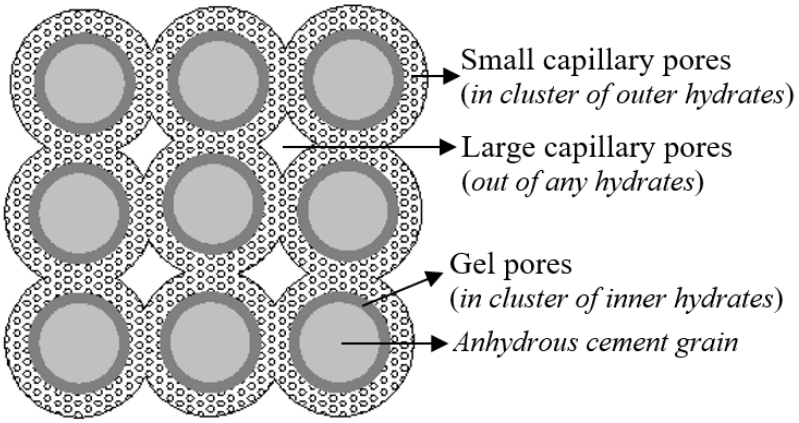

740

741 Figure 9. A sketch of the microstructure in hydrated cementitious systems.

742

743

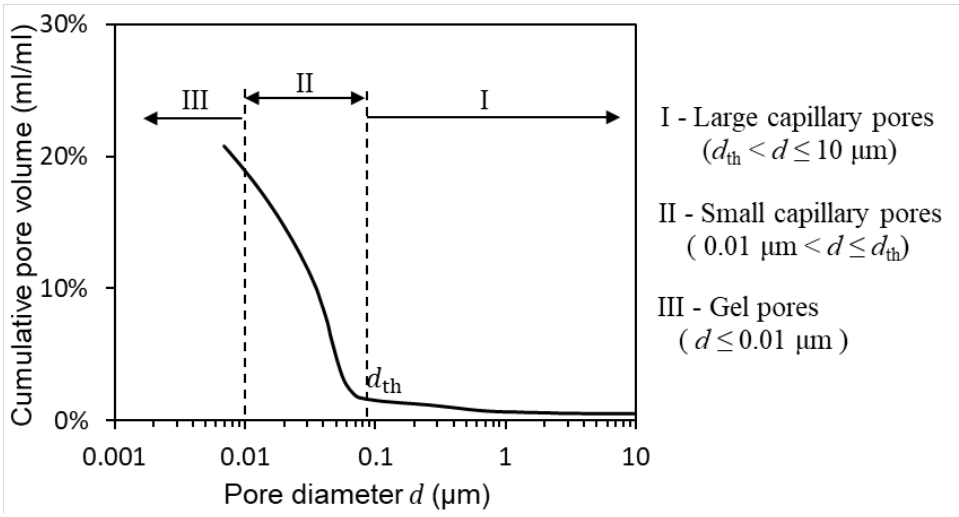

744

745 Figure 10. Three pore categories based on MIP-derived pore size distribution. d_{th} - threshold
746 pore diameter.

747

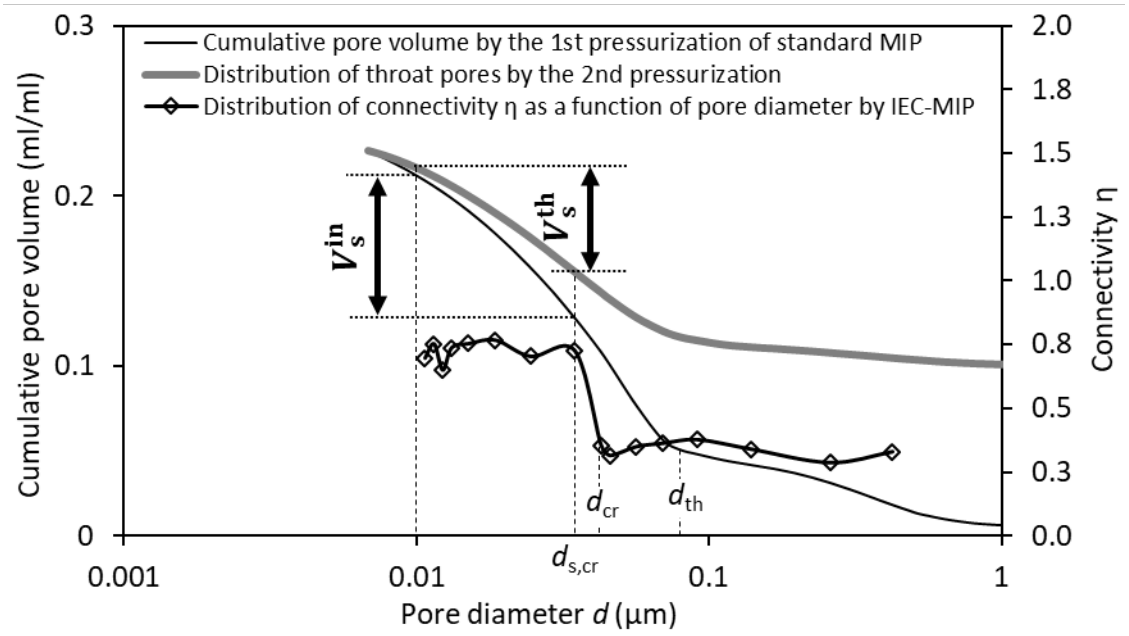

748

749 Figure 11. Determination of the connectivity η_{sc} of small capillary pores (range II: 0.01 μm <
750 $d \leq d_{th}$) in cement paste (w/b = 0.4, 28-day-old). d_{th} – threshold pore diameter; d_{cr} – critical
751 pore diameter; $d_{s,cr}$ is the pore diameter smaller than, but close to, the critical pore diameter d_{cr}.

752

753

754

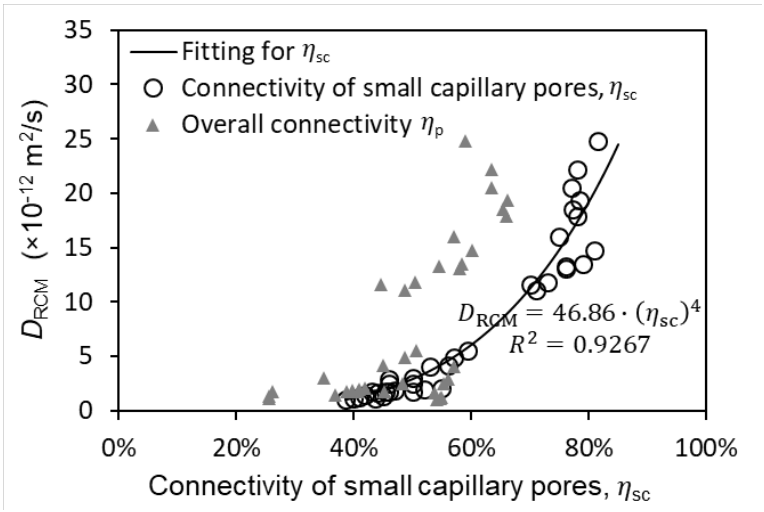

755

756 (a)

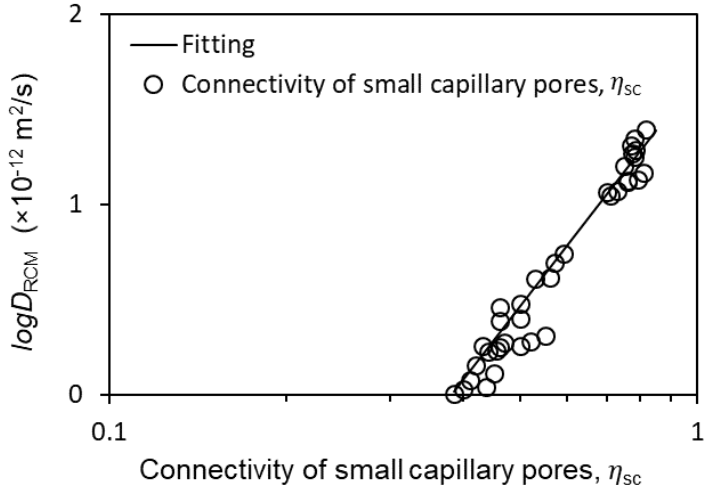

757

758 (b)

759 Figure 12. (a) Power relationship between chloride migration coefficient D_{RCM} and
760 connectivity η_{sc} of small capillary pores (0.01 μm < $d \leq d_{th}$), regardless of the binders (OPC
761 and blends); (b) Relationship between logD_{RCM} and η_{sc} in logarithmic plots.

762

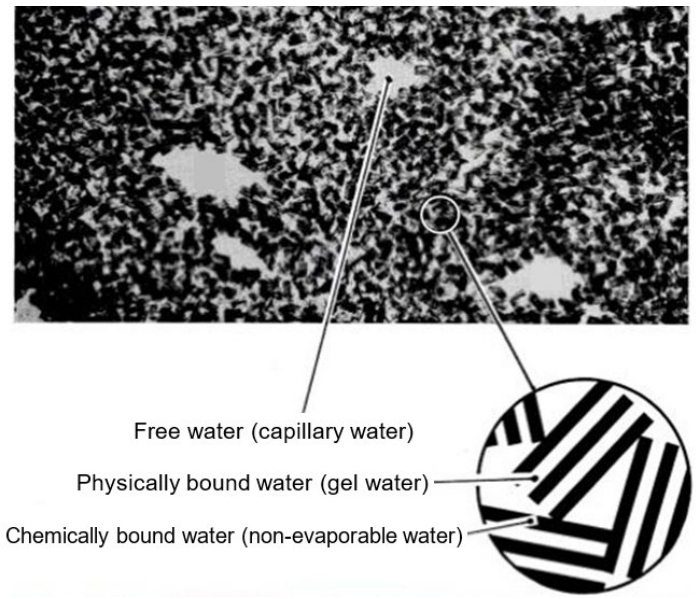

763

764 Figure 13. Illustration of water phases in the cement paste [55].

765

766

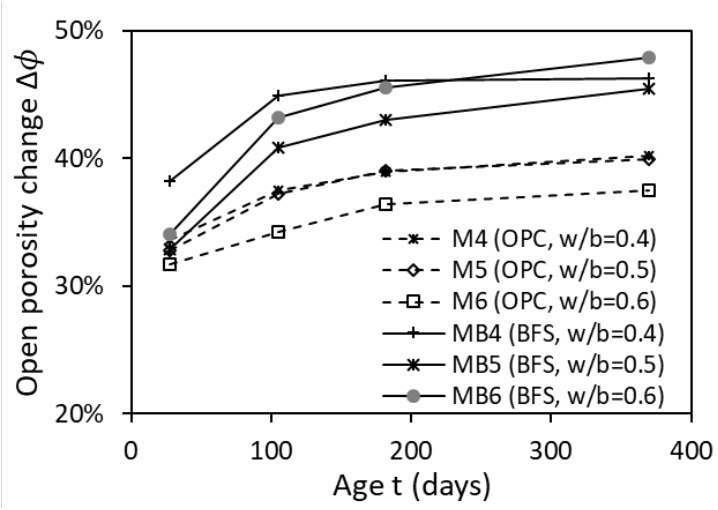

767

768 Figure 14. Open porosity change ($\Delta\phi(t) = \phi_0 - \phi_t$) with age for OPC and BFS-blended
769 pastes with w/b of 0.4, 0.5 and 0.6. ϕ_0 is the initial porosity according to Eq. (10) and ϕ_t is
770 the total open porosity by mercury porosimetry measurements.

Tables

Table 1. Mix proportions for paste and mortar samples (weight percentage) with ordinary Portland cement (OPC), fly ash (FA), ground granulated blast furnace slag (BFS) and limestone powder (LP).

Mixtures	water-binder-ratio (w/b)	OPC	FA	BFS	LP
M4	0.4	100%			
M5	0.5	100%			
M6	0.6	100%			
MF5	0.5	70%	30%		
MFL5	0.5	65%	30%		5%
MB4	0.4	30%		70%	
MB5	0.5	30%		70%	
MB6	0.6	30%		70%	
MBL5	0.5	25%		70%	5%

Table 2. Overall connectivity η_p of paste mixtures obtained by standard MIP tests.

Mixtures	Age (days)			
	28	105	182	370
M4	54.5%	50.5%	47.0%	45.1%
M5	60.1%	58.4%	57.3%	57.1%
M6	66.1%	66.0%	65.5%	63.4%
MF5	58.9%	50.6%	48.3%	45.8%
MFL5	61.7%	57.7%	55.2%	55.1%
MB4	34.8%	26.1%	25.9%	25.3%
MB5	45.0%	39.7%	38.8%	37.3%
MB6	48.6%	41.8%	40.8%	40.7%
MBL5	56.0%	54.9%	54.6%	54.4%

782 Table 3. Initial porosity ϕ_0 of paste mixtures according to Eq. (10).

Mixtures	M4	M5	M6	MF5	MFL5	MB4	MB5	MB6	MBL5
ϕ_0	55.5%	61.0%	65.2%	58.3%	58.3%	54.1%	59.5%	63.8%	59.5%

783